PCCP

PAPER

View Article Online
View Journal

Cite this: DOI: 10.1039/d6cp01072e

Phase behaviour of liquid CO_2 with an impurity of water: influence of CO_2 hydrate

Hideki Tanaka, *[ab] Masakazu Matsumoto, [a] Takuma Yagasaki, [c] Munetaka Takeuchi, [b] Yoshihito Mori [d] and Takumi Kono [b]

Received 24th March 2026,
Accepted 20th May 2026

DOI: 10.1039/d6cp01072e

rsc.li/pccp

The solubility of water in liquid CO_2 coexisting with CO_2 hydrate or liquid water is evaluated in order to investigate the thermodynamic conditions to avoid the formation of CO_2 hydrate in the transportation processes of liquid CO_2. To this end, theoretical calculations have been carried out to obtain the chemical potentials of water and CO_2 in all the phases involved in their coexistence. The solubility of water in liquid CO_2 coexisting with liquid water decreases with decreasing temperature over a wide range of temperature and pressure, except for in the vicinity of the critical point of CO_2. The decrease in the solubility is further enhanced by the formation of hydrate. We estimate the Gibbs energy of hydrate formation, which is an important property for sequestration of CO_2, for cases where the temperature or pressure of water-saturated liquid CO_2 decreases. We also estimate the amount of water precipitated as hydrate during these processes, which has a direct bearing on flow assurance in CO_2 transportation. The present study will contribute to the development of a low-energy, safe CO_2 transport network aiming at achieving large-scale carbon neutrality.

Introduction

Carbon dioxide (CO_2) is often used in industries as a non-toxic solvent to extract precious substances, mostly under supercritical conditions.[1] Advantage is taken of the fact that its critical temperature, 304.2 K, is well within the room temperature range and supercritical CO_2 acts as a good solvent for a variety of substances. It is also utilised as a cooling agent owing to the large latent heat of the sublimation of dry ice, 25 kJ mol^{-1},[2] which is associated with its triple point pressure (0.517 MPa) being higher than atmospheric pressure.[3]

One of the key concerns regarding CO_2 is how emitted greenhouse gases can be reduced through CO_2 capture and storage (CCS).[4] Formation of clathrate hydrate (hereafter hydrate) at low temperatures and high pressures poses a potential risk of causing pipeline blockage during transportation of CO_2 containing water as an impurity in the CCS process.[5] It is possible to suppress hydrate formation by dosing with kinetic inhibitors such as polyvinyl caprolactam or thermodynamic inhibitors such as methanol. Extensive efforts have been devoted to finding efficient inhibitors and exploring possible mechanisms for the inhibitors to work.[6–10] Another way is the removal of water prior to transportation. To implement this strategy to exploit safe and feasible CCS, it is an urgent task to gain a comprehensive understanding of the various features of water dissolved in liquid CO_2.

A hydrate is a crystal composed of water molecules forming a host lattice structure in which small guest molecules are encapsulated.[11] It is a nonstoichiometric compound with respect to guest composition, *i.e.*, the number of guest molecules in the host lattice. Its thermodynamic stability and composition of the guest significantly depend on temperature and pressure. We have studied the thermodynamic stabilities of hydrates encaging various kinds of guest species based on atomistic models of intermolecular interactions.[12–18] Our theory stems from the van der Waals and Platteeuw (vdWP) theory[19–21] originally developed to predict three-phase coexistence (water, hydrate, and guest fluid phases) but is different in the ensemble to which the relevant partition function is linked. The free energy derived from our theory enables the evaluation of the two two-phase coexistences between the hydrate and aqueous phases and between the hydrate and guest fluid phases. We reveal that this approach, which requires only a few empirical parameters, plays a significant role in achieving this objective.

Hydrates have been utilised for storing various gases of small molecular size, desalination of seawater, and energy resources.[11] Natural CH_4 hydrate is expected to be an energy resource. Recovering CH_4 from hydrate is essential to mitigating

[a] Research Institute for Interdisciplinary Science, Okayama University, Okayama 700-8530, Japan. E-mail: htanakaa@okayama-u.ac.jp
[b] Engineering Advancement Association of Japan, 1-11-9 Azabudai, Minato-ku, Tokyo 105-0001, Japan
[c] Division of Chemical Engineering, Graduate School of Engineering Science, Osaka University, Osaka 560-8531, Japan
[d] Ochanomizu University, 2-1-1 Ohtsuka, Bunkyo-ku, Tokyo 112-8610, Japan

global warming; otherwise, the release of CH_4 into the atmosphere from the hydrate accelerates it because CH_4 has a stronger greenhouse effect than CO_2 does. Replacing CH_4 in hydrate with CO_2 may provide an efficient way to contribute to CCS. Hence, the phase behaviour of CH_4 hydrate would also be a key issue in CCS.

The solubility of water in liquid CO_2 is an important property for CCS. Although a fairly large amount of measured solubility data has been accumulated,[22,23] the solubility values depend on individual measurements, and the deviation among them is considerably large. The solubility of water in liquid CO_2 is approximately on the order of 10^{-3} in mole fraction at 280 K around a pressure of 10 MPa, which is one order lower than that of CO_2 in liquid water.[24,25] A serious concern that has not been fully addressed is the influence of hydrate formation on the solubility. Liquid CO_2 coexists with water in the high-temperature and low-pressure region, while it coexists with CO_2 hydrate in the low-temperature and high-pressure region. We have developed a method to evaluate the solubility under the coexistence of hydrate taking into account the change in the chemical potential of water due to the formation of hydrate.[17] We expect that an application of this method to an extended range of thermodynamic conditions could be useful for the practical transportation and storage of liquid CO_2 containing water.

In the present study, we address the following three issues. First, the solubility of water in liquid CO_2 is calculated in the presence or absence of hydrate. Our calculations are performed in a temperature range between 220 and 325 K and at pressures of 5, 10, 20, 30, 50 and 100 MPa. In contrast to our previous study,[17] this range includes temperatures and pressures above the critical point of CO_2. This extent of the coverage is essential since some operations in CO_2 transportation would be made under such conditions to avoid bubbling. Next, we examine various properties of CO_2 hydrate that affect the thermodynamic properties of the coexisting phases and compare them with those of CH_4 hydrate obtained in our previous studies.[14–16] Finally, we investigate the amount of CO_2 hydrate formed from a supersaturated state prepared by rapid cooling or decompression along with the corresponding formation Gibbs energy of the hydrate.

Theory and methods

Since we have presented most of the methods to calculate the phase behaviours of CO_2 hydrate and the solubility of water in our previous papers,[14–18] they are described below only briefly. A CO_2 hydrate coexists with either an aqueous solution or a CO_2-rich liquid. The compositions in the aqueous solution and liquid CO_2 are denoted by z'_c (mole fraction of CO_2) and $z''_w = 1 - z''_c$ (mole fraction of water), respectively. Those in CO_2 hydrate are represented by the mole fraction of CO_2 as y'_c on the phase boundary between the aqueous solution and the hydrate (water/hydrate boundary) and as y''_c on the phase boundary between the hydrate and liquid CO_2 (hydrate/CO_2 boundary).

Thermodynamic conditions for hydrate formation

The phase behaviour of CO_2 hydrate is represented in the space of temperature, T, pressure, p, and composition, y. The original vdWP theory was proposed to calculate the dissociation pressure of hydrate at the three-phase equilibrium, where the water, hydrate, and liquid CO_2 phases coexist in a certain range of temperature.[19] Actually, it is a locus of the intersections between the two two-phase boundaries (water/hydrate and hydrate/CO_2) projected onto the T–p plane.[12,13] The dissociation pressure for CO_2 hydrate is depicted against temperature in Fig. 1. The present theoretical calculation successfully agrees with experimental measurements.[26–28] The upper-left area delimited by the curve is the stable zone of the hydrate. The highest temperature of the three-phase coexistence for CO_2 hydrate is around 297 K.

The agreement of the dissociation pressures at high pressure is moderate compared with those at low pressures in the range of $p < 20$ MPa. Although the reentrant character in the experimental observations is reproduced by our theoretical calculations, the deviation from experimental measurement becomes large in the very high-pressure region above 200 MPa. As will be described below, the equilibrium condition is determined using the chemical potential of ice Ih. However, this ice is no longer stable under such high pressures. Thus, it is reasonable to consider that our calculations are sound and at least semi-qualitatively correct at pressures lower than ~100 MPa.

Phase diagram for binary mixture of water and CO_2

In Fig. 2, we display a global phase diagram of the binary mixture of water and CO_2 at 10 MPa. This figure shows all the phases in T–y space involved in the present study. The stable phase at the low composition of CO_2 is the aqueous solution occupying the left region separated by the blue line. It shrinks to zero below the freezing temperature of water for no

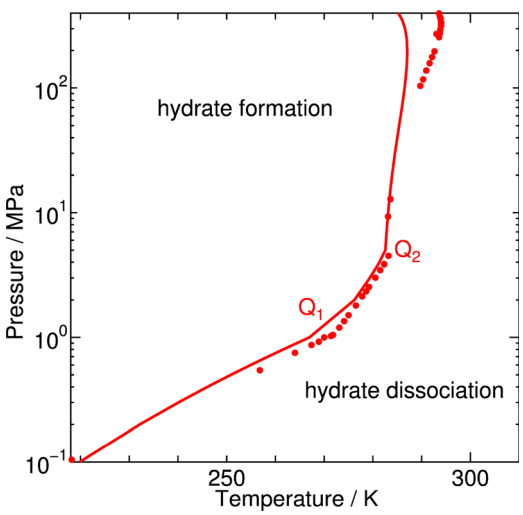

Fig. 1 Dissociation pressure of CO_2 hydrate, by which the CO_2 hydrate formation and dissociation zones are separated, obtained from theoretical calculations (solid line). Experimental results are shown by filled circles.

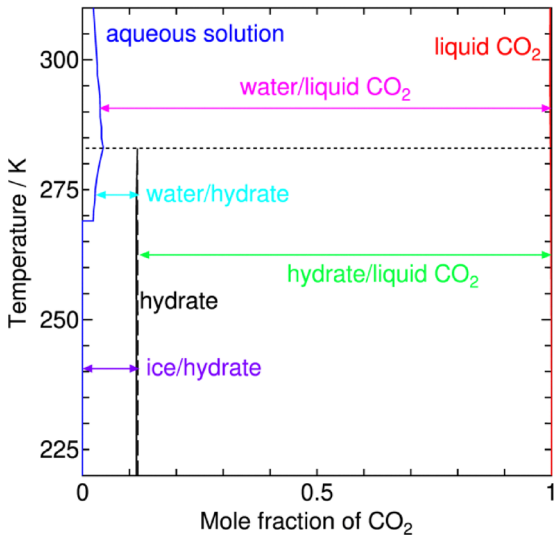

Fig. 2 Phase diagram of the binary mixture of water and CO_2 at 10 MPa. The boundaries of the stable phases are represented by a blue line for the aqueous solution, black lines for the hydrate, and red line for liquid CO_2. The horizontal dotted line indicates the dissociation temperature of CO_2 hydrate.

incorporation of CO_2 in ice. The stable phase in the middle is the hydrate phase, which is not given as a single line but is surrounded by the boundary of the aqueous solution with the hydrate (water/hydrate) and that of the hydrate with the CO_2-rich solution (hydrate/CO_2). The CO_2-rich solution including the gaseous phase, called hereafter liquid CO_2, exists at high composition of CO_2, though it occupies only a narrow region beyond the red line. When the temperature is higher than the dissociation temperature denoted by the horizontal dotted line, no hydrate forms, and the aqueous phase coexists with liquid CO_2 (water/CO_2). The hydrate intervenes between the aqueous phase and the liquid CO_2 phase below the dissociation temperature. Each phase boundary is determined by the equivalence of the chemical potential of either water or CO_2 between the two phases. CO_2 is regarded as the solute species in the aqueous solution, while it is treated as the solvent in liquid CO_2. The hydrate, guest liquid, aqueous, and ice phases are designated by the superscripts (hy), (lq), (aq), and (ice) in the following description of the phase equilibria.

Liquid CO_2 in equilibrium with aqueous solution without CO_2 hydrate

First, we consider the thermodynamic conditions where T is high and/or p is low, and therefore CO_2 hydrate is not formed. Liquid CO_2 is in direct contact with the aqueous solution. It is assumed that the chemical potential of water in the aqueous solution, $\mu_w^{(aq)}(T,p,z_c')$, can be approximated to that of pure water, $\mu_w^0(T,p)$. Likewise, that of CO_2 in liquid CO_2, $\mu_c^{(lq)}(T,p,z_c'')$, is assumed to be equal to that of pure liquid CO_2, $\mu_c^0(T,p)$. The rationale of these approximations is based on the low mutual solubilities.[22–25] The methods to calculate the chemical potentials of the two pure substances are given elsewhere.[17] The equilibrium condition for each two-phase coexistence is calculated from

$$\mu_j^0(T,p) = \mu_j^{(k)}(T,p,z) = k_B T \ln(\rho_j \lambda_j^3) + \mu_j^e(T,p) + f_j^{(r)}(T), \quad (1)$$

where k_B denotes the Boltzmann constant and $\mu_j^{(k)}(T,p,z)$, ρ_j, λ_j, $f_j^{(r)}$, and $\mu_j^e(T,p)$ stand for the chemical potential in solvent k, number density, thermal de Broglie wavelength, free energy of the rotational motion of the rigid model for the solute, and excess chemical potential arising from the interaction of the solute with surrounding solvent molecules for species j. The excess chemical potential, $\mu_j^e(T,p)$, is calculated assuming infinite dilution of the solute in the solvent of the counterpart species. In the practical calculation, the density of the solute is given by

$$\rho_j(T,p) = \lambda_j^{-3} \exp\left[\frac{\mu_j^0(T,p) + \varepsilon_j - \mu_j^e(T,p) - f_j^{(r)}(T)}{k_B T}\right], \quad (2)$$

where ε_j is an energy correction associated with self-polarization. It is set to 7.8 kJ mol^{-1} for $j = w$ (water) with the TIP4P/ice model and 0 kJ mol^{-1} for $j = c$ (CO_2) with the TraPPE model, accounting for the different environments.[17,29,30] The solubility of solute species j in solvent k is

$$z_j(T,p) = \frac{\rho_j(T,p)}{\rho_j(T,p) + \rho^{(k)}(T,p)} \approx \frac{\rho_j(T,p)}{\rho^{(k)}(T,p)}, \quad (3)$$

where $\rho^{(k)}$ is the density of the pure liquid k.

CO_2 hydrate in equilibrium with either aqueous solution or liquid CO_2

Cooling and compression promote the formation of CO_2 hydrate. Such a hydrate has the two boundaries in the composition (mole fraction) space at a given T and p. It coexists with the aqueous phase on one boundary at y' and with the liquid CO_2 phase on the other boundary at y''.

The water/hydrate boundary is obtained from the equivalence of the chemical potentials of water in the aqueous solution and in the hydrate as

$$\mu_w^{(hy)}(T,p,y_c') = \mu_w^0(T,p). \quad (4)$$

The chemical potential of water changes by $\Delta\mu_w^{(hy)}$ while traversing from the water/hydrate boundary fixed by eqn (4) to the hydrate/CO_2 boundary. The chemical potential of water on the hydrate/CO_2 boundary is given by

$$\mu_w^{(hy)}(T,p,y_c'') = \mu_w^0(T,p) + \Delta\mu_w^{(hy)}, \quad (5)$$

which should be equal to $\mu_w^{(lq)}(T,p,z_c'')$.[13,16]

On the hydrate/CO_2 boundary, the chemical potential of CO_2 in the hydrate equals that in the liquid CO_2 phase. The composition in the hydrate on this boundary is calculated from

$$\mu_c^{(hy)}(T,p,y_c'') = \mu_c^0(T,p). \quad (6)$$

The chemical potential of CO_2 changes by $\Delta\mu_c^{(hy)}$ due to the decrease in composition from the hydrate/CO_2 boundary determined by eqn (6) to the water/hydrate boundary. The chemical

potential of CO_2 on the water/hydrate boundary is given as

$$\mu_c^{(hy)}(T,p,y_c') = \mu_c^0(T,p) + \Delta\mu_c^{(hy)}, \quad (7)$$

which should be equal to $\mu_c^{(aq)}(T,p,z_c')$.[17]

Eqn (5) and (7) have the same form. Therefore, the density of CO_2 in the liquid water phase and the density of water in the liquid CO_2 phase in the presence of the hydrate are calculated using the common form given by

$$\rho_j(T,p) = \lambda_j^{-3}\exp\left[\frac{\mu_j^0(T,p) + \varepsilon_j + \Delta\mu_j^{(hy)} - \mu_j^e(T,p) - f_j^{(r)}(T)}{k_BT}\right]. \quad (8)$$

Excess chemical potential of water in liquid CO_2

The excess chemical potential of solute species j is calculated according to the particle insertion[31] as

$$\mu_j^e(T,p) = -k_BT\ln\left[\frac{\left\langle V\exp\left(-\phi_j/k_BT\right)\right\rangle_{T,p}}{\langle V\rangle_{T,p}}\right], \quad (9)$$

where ϕ_j is the interaction potential energy of a randomly inserted solute molecule with all the surrounding solvent molecules and V indicates the volume of the pure solvent. A molecular dynamics (MD) simulation is performed for 5 to 110 ns to generate molecular coordinates at each T and p for liquid water and CO_2.[32–34] The numbers of water and CO_2 molecules are set to 1024 and 864, respectively. The number of solute insertions is maximally 8×10^{12} for each thermodynamic condition. All the intermolecular interactions are smoothly truncated at 1.2 nm by multiplying a switching function[35] so that the lattice dynamics for the free energy calculation of the host hydrate and ice[36] are performed without suffering from the discontinuities associated with the abrupt cutoff of the interaction.

Composition of CO_2 hydrate

The vdWP theory[19] establishes a relation between the occupancy of a cage of type j, x_j, and the chemical potential of water in hydrate, $\mu_w^{(hy)}(T,p,y)$, with the aid of the chemical potential of water in empty hydrate, $\mu_h^0(T,p)$, as

$$\mu_w^{(hy)}(T,p,y) = \mu_h^0(T,p) + k_BT\sum_j \alpha_j\ln(1-x_j), \quad (10)$$

where α_j is the ratio of the number of j type cages to the number of water molecules. This is applicable even to a thermodynamic condition where only the hydrate exists as a stable phase.[12–18] The occupancy is calculated according to

$$x_j = \frac{\exp\left[\frac{(\mu_g - f_j)}{k_BT}\right]}{\exp\left[\frac{(\mu_g - f_j)}{k_BT}\right] + 1} \quad (11)$$

where μ_g and f_j stand for the chemical potential of the guest in the hydrate and the free energy of occupation of the type j cage, which is either large 14- or small 12-hedron for CS-I CO_2 hydrate. The free energy of cage occupation, f_j, for the linear rigid CO_2 molecule is given by

$$f_j = -k_BT\ln\left[\left(\frac{2\pi mk_BT}{h^2}\right)^{\frac{3}{2}}\frac{2\pi Ik_BT}{sh^2}\iint\exp\left(-\frac{\psi_j(\mathbf{R},\mathbf{\Omega})}{k_BT}\right)d\mathbf{R}d\mathbf{\Omega}\right], \quad (12)$$

where m and I are the mass and the moment of inertia, h is the Planck constant, and s is the symmetry number, which is 2 for CO_2. In this equation, $\psi_j(\mathbf{R},\mathbf{\Omega})$ represents the interaction energy of the guest CO_2 molecule at position $\mathbf{R}$ and orientation $\mathbf{\Omega}$ with all surrounding water molecules. The free energy of cage occupation is significantly affected by the host–guest interaction and the shape of the cage. A set of occupancies, x_j, is connected with the composition, y, as

$$y = \frac{\sum_j \alpha_j x_j}{\sum_j \alpha_j x_j + 1}. \quad (13)$$

One of the significant differences from the original vdWP theory is that the chemical potential of guest species in the hydrate is calculated from eqn (13) combined with eqn (11) *via* the occupancies for each given composition, y. The chemical potential of the guest species in eqn (11) is substituted with that in its pure fluid state to determine the hydrate/CO_2 boundary using eqn (10).[12,13,29]

Chemical potentials of ice, empty hydrate, and liquid water

The chemical potential of occupied hydrate is calculated according to eqn (10) once that of the empty hydrate and the occupancies are given. The free energy of empty hydrate, $A(T,V,N_w)$, is assumed to be the sum of the cohesive energy, $U_q(V,N_w)$, the harmonic vibrational free energy, $F_H(T,V,N_w)$, and the residual entropy term, $TS_r(N_w)$, given as[18]

$$A(T,V,N_w) = U_q(V,N_w) + F_H(T,V,N_w) - TS_r(N_w). \quad (14)$$

The harmonic vibrational free energy is calculated from a set of the frequencies, ν_j, as

$$F_H(T,V,N_w) = k_BT\left\langle\sum_j \ln\left(\frac{h\nu_j}{k_BT}\right)\right\rangle, \quad (15)$$

where $\langle\rangle$ indicates the average over the generated hydrogen-disordered structures. The residual entropy does not affect the phase boundary since it is a function of only N_w. To obtain the equilibrium volume, $\langle V\rangle$, the following function is minimized with respect to V:

$$Y(T,V,N_w,p) = A(T,V,N_w) + pV. \quad (16)$$

The chemical potential of empty hydrate, $\mu_h^0(T,p)$, is simply calculated as

$$\mu_h^0(T,p) = \frac{A(T,\langle V\rangle,N_w) + p\langle V\rangle}{N_w}. \quad (17)$$

The same method is used to calculate the chemical potential of ice Ih. The anharmonic free energies of ice and hydrate are likely to be comparable. Since this component cancels out in eqn (4), we exclude it from eqn (14).

An extension to higher temperatures beyond the melting point of ice is required. The chemical potential of pure liquid water, $\mu_w^0(T,p)$, at temperature $T = T_m + \Delta T$ and pressure p can be estimated as

$$\mu_w^0(T,p) \approx \mu_{ice}(T,p) - \Delta s(T_m,p)\Delta T - \frac{\Delta c_p(T_m,p)}{2T_m}\Delta T^2, \quad (18)$$

where $\Delta s(T_m,p)$ and $\Delta c_p(T_m,p)$ are the differences in the entropy and heat capacity per molecule at constant pressure between ice and liquid water. Those properties are rather easily calculated from MD simulations.[18]

The phase boundary between water and hydrate is found by equating the chemical potential of water in hydrate in eqn (10) with that of ice (or liquid water) according to eqn (4). The occupancy at this equilibrium is calculated from eqn (11) and (13). The other boundary between hydrate and guest species is given by the equivalence of the chemical potential of the guest species according to eqn (6).

Intermolecular interactions and structures of hydrate and ices

A hydrate is composed of host water and guest molecules. The water–water interaction is described by the TIP4P/ice model,[29] which is superior in reproducing the melting temperature of ice Ih and several properties of hydrates.[37,38] We adopt the TraPPE model for CO_2,[30] which is a rigid rotor with three interaction sites, and the united-atom OPLS model for CH_4.[39] The capability of this CO_2 model to recreate the phase diagram around the triple point gives a rationale for its use under CO_2-rich conditions instead of other models.[40,41] Those parameters are listed in Table 1. A deviation from the Berthelot rule is introduced for the Lennard-Jones (LJ) interactions of the unlike pairs of molecules,[13,16,42–44] while the Lorentz rule is always applied. A scaling factor, χ, is multiplied to the LJ energy parameter value from the Berthelot rule to recover the experimental dissociation pressure around 273 K.

One hundred hydrogen-disordered CS-I structures are generated using the GenIce tool[45,46] for the calculation of the free energy and other properties of the hydrate. The CS-I structure consists of 368 water molecules. The generated configurations satisfy the ice rules having no net polarization.[47,48] The chemical potentials of ice, empty hydrate, and liquid water were calculated previously.[12–17]

Table 1 Potential models for CO_2 and CH_4. Partial charge (q), LJ size parameter (σ), and LJ energy parameter (ε) used in the models. A scaling factor, χ, is multiplied by the value obtained from the Berthelot rule for interactions with the oxygen atom of water. The C–O distance is fixed to 0.1160 nm

Site	q/e	σ/nm	ε/kJ mol^{-1}	χ
C	0.7000	0.2800	0.2245	1.13
O	−0.3500	0.3050	0.6568	1.13
CH_4	0.0	0.3730	1.231	0.980

Results and discussion

Solubilities of CO_2 in water and water in liquid CO_2

In Fig. 3, we show the solubility of CO_2 in the aqueous phase and the solubility of water in the liquid CO_2 phase at 10 MPa. The aqueous phase is assumed to be in equilibrium with the hydrate or liquid CO_2 in the whole range of temperature examined here, while the liquid CO_2 is assumed to be in equilibrium with the hydrate or aqueous solution. Thus, each curve is extended to the range of the metastable state.[17] As the temperature increases, the solubility curve shifts from the solid one to the dotted one at the crossover, the three-phase coexistence condition, indicated by the arrow. The agreement with the experimental measurements[22] is excellent in the solubility of water in liquid CO_2 once an appropriate value of the self-polarization energy of the TIP4P/ice[29] model, ε_w = 7.8 kJ mol^{-1}, is chosen.[17] The experimental values at 0.1 MPa[24,25] are compared to the theoretical ones in the inset of Fig. 3. The solubility of CO_2 is reproduced within the range of accuracy required for our later discussion.

The solubility of CO_2 in liquid water coexisting with liquid CO_2 decreases with rising temperature. This behaviour is commonly observed in the solubility of a solute substance having a low boiling point. However, the solubility increases with rising temperature when the aqueous solution coexists with CO_2 hydrate. The crossover of the solubility curves against temperature has also been observed experimentally.[49] The difference in the solubility between the dotted and solid curves arises from the decrease in the chemical potential of CO_2 associated with traversing from the hydrate/CO_2 boundary to the water/hydrate boundary in composition space, $\Delta\mu_c^{(hy)}$ in eqn (7).[13,16]

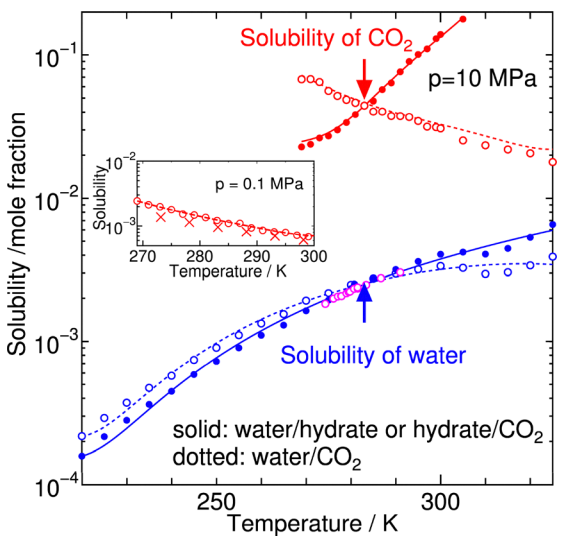

Fig. 3 Solubility of CO_2 in the aqueous solution (red) and that of water in the liquid CO_2 (blue) in the presence (solid line) and absence (dotted line) of CO_2 hydrate plotted against temperature at 10 MPa. The crossover of the coexistence curve is indicated by the arrow. Experimental values of the solubility of CO_2 at 0.1 MPa (cross) are compared to the theoretical ones (open circle and dotted line) in the inset. The magenta open circles are experimental values of the solubility of water at 10.1 MPa.[22]

From a qualitative viewpoint, this is accounted for simply by the fact that the mole fraction of CO_2 on the water/hydrate boundary is lower than that on the hydrate/CO_2 boundary. As for the solubility of water in liquid CO_2, the chemical potential of water on the water/hydrate boundary is higher, and therefore the solubility of water in the presence of the hydrate is lower than the value in the absence of the hydrate. A more quantitative argument on the difference in the solubility between CO_2 and water will be made below in relation to the phase behaviours of the CO_2 hydrate.

The solubility curves excluding the metastable regions are depicted in Fig. 4a. The agreement with experiments at 10.1 MPa is remarkably good, as shown previously.[17,22] The solubility of CO_2 in the absence of hydrate considerably depends on temperature. Formation of the hydrate not only changes the sign of the slope against temperature but also decreases the magnitude of the pressure dependence, as seen in Fig. 4a.[16] This trend is also observed in experimental measurements.[50] On the other hand, the formation of hydrate alters to some extent the slope of the solubility curve of water against temperature.[17] Compression leads to a higher solubility of water even in the presence of hydrate.[22,51]

The standard deviations are calculated for the solubilities of water in CO_2 by dividing a set of excess chemical potential values into 10 blocks. The error bars are shown in Fig. 4b. The standard deviations are fairly large at 100 MPa, which arises from the fact that particle insertion is difficult for very condensed liquids. On the other hand, those at low pressures such as 10 MPa are small. Fig. S1 demonstrates that our MD simulations are sufficiently long to obtain statistically reliable results even near the critical point where the molar volume fluctuates to a large extent.

It is appropriate to compare our results with solubility curves obtained from the fitting of accumulated experimental measurements.[23] This comparison is made in Fig. 4b. The results are not in good agreement with ours unlike those by Seo *et al.*[22] However, it is noted that the individual measurements used for the fitting differ from each other. In fact, the solubility values at 285 K and 10 MPa vary among sources: approximately 2.8×10^{-3} in the present study and ref. 22, 2.0×10^{-3} in ref. 23, and 2.6×10^{-3} in ref. 52 where an equation of state was used to calculate the solubility. This inevitably leads to a fairly large error. Therefore, we must be satisfied with the situation that the general features of the temperature and pressure dependence are at least semi-qualitatively reproduced. Another key issue in the fitting method is that the break in the solubility curve resulting from hydrate formation is effectively averaged out within a single smoothed curve.

Nonstoichiometric properties of CO_2 hydrate

We examine some properties of hydrates which affect the solubility curve due to the non-stoichiometric nature characteristic to hydrates. Here, we compare our results for CO_2 hydrate with those for CH_4 hydrate. While CH_4 hydrate was examined in our previous work[14,15] using the OPLS model,[39] the results for CO_2 are newly obtained using the TraPPE model,[30] which is capable of reproducing the phase behaviour of pure CO_2 and therefore is advantageous to describing liquid CO_2 containing a tiny amount of water.

One of the intriguing properties representing the non-stoichiometry of hydrates is the number of water molecules per guest species, called the hydration number. It has often been explored in studying the composition of hydrates.[53,54] The pressure and temperature dependences of the hydration numbers along the three-phase coexistence curve are depicted for CO_2 and CH_4 hydrates in Fig. 5. The hydration number of CO_2 hydrate is generally large. It decreases with compression for CO_2 hydrate, while it has a peak around 3 MPa for CH_4 hydrate.

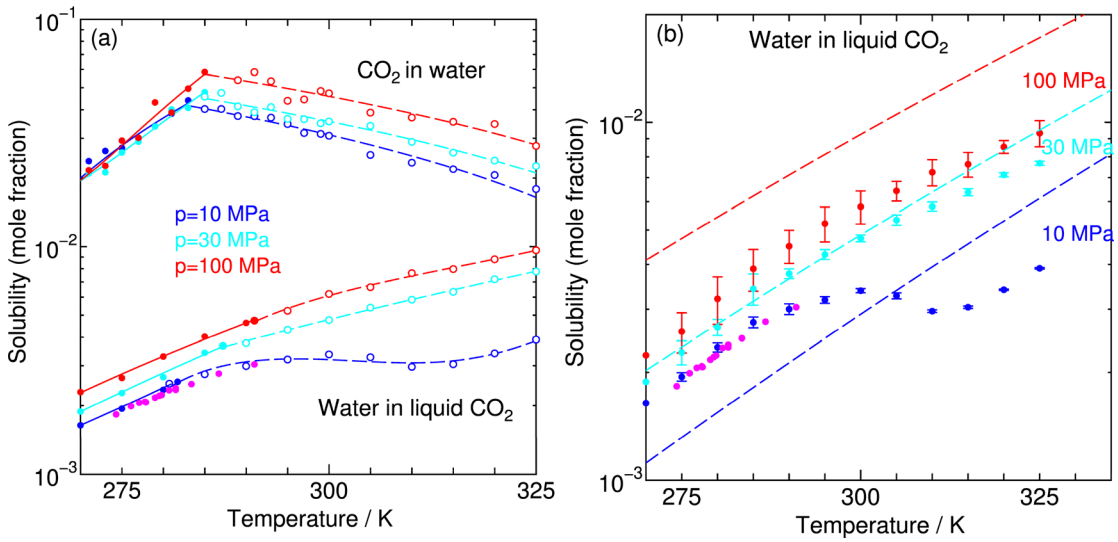

Fig. 4 (a) Solubilities of CO_2 in liquid water (upper) and water in liquid CO_2 (lower) at 10 (blue), 30 (cyan), and 100 (red) MPa in the presence (solid line) and absence (dashed line) of CO_2 hydrate plotted against temperature along with those obtained from experimental measurements at 10.1 MPa (magenta circle).[22] (b) Solubilities of water in liquid CO_2 with error bars at the same pressures along with those obtained from the fitting of experimental data (dashed line).[23]

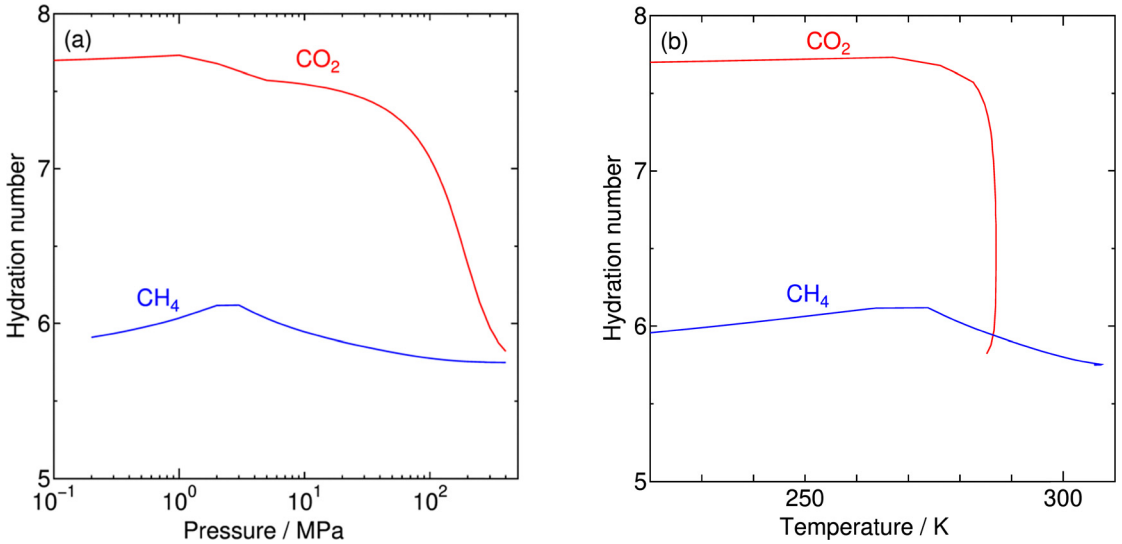

Fig. 5 Hydration numbers of (red) CO_2 and (blue) CH_4 hydrates along the three-phase coexistence curve as a function of (a) pressure and (b) temperature.

While the hydration number of CO_2 hydrate relies heavily on the condition (temperature or pressure), that of CH_4 hydrate is rather constant.[53] The three-phase coexistence pressure of CO_2 hydrate increases with temperature significantly around 280 K, as shown in Fig. 1. High pressure inevitably leads to encapsulation of the small cages. This results in the abrupt drop of hydration number in CO_2 hydrate shown in Fig. 5.

CO_2 hydrate forms spontaneously in the upper-left area of the dissociation curve in Fig. 1. When the pressure is fixed at a certain value, the hydrate is in equilibrium with either the aqueous phase or the liquid CO_2 phase depending on the composition. The aqueous solution coexists on the water/hydrate boundary while the liquid CO_2 phase does on the hydrate/CO_2 boundary. These two types of boundaries in temperature (T)–composition (y) space are depicted in Fig. 6a, and the corresponding results for CH_4 hydrates are shown in Fig. 6b. The size of the stable region of CO_2 hydrate in the T–y plane is comparable to that of CH_4 at low pressures. The shape of the region, however, differs from that of CH_4 and looks rather like that of C_2H_6 hydrate.[13,18] The area increases with increasing pressure due to the gradual encapsulation of CO_2 molecules in the small cages, and, therefore, the extent of increase by compression is more pronounced than that for CH_4 hydrate. The composition of the enclosed region for CO_2 hydrate calculated with the TraPPE model[14,16,30] is lower than that estimated from a different potential model.[55] The water/hydrate boundary curve has a break caused by the melting of ice except for at 1 MPa. The formation of hydrate rather than ice is a practical concern for flow assurance in the high-pressure region having the break.

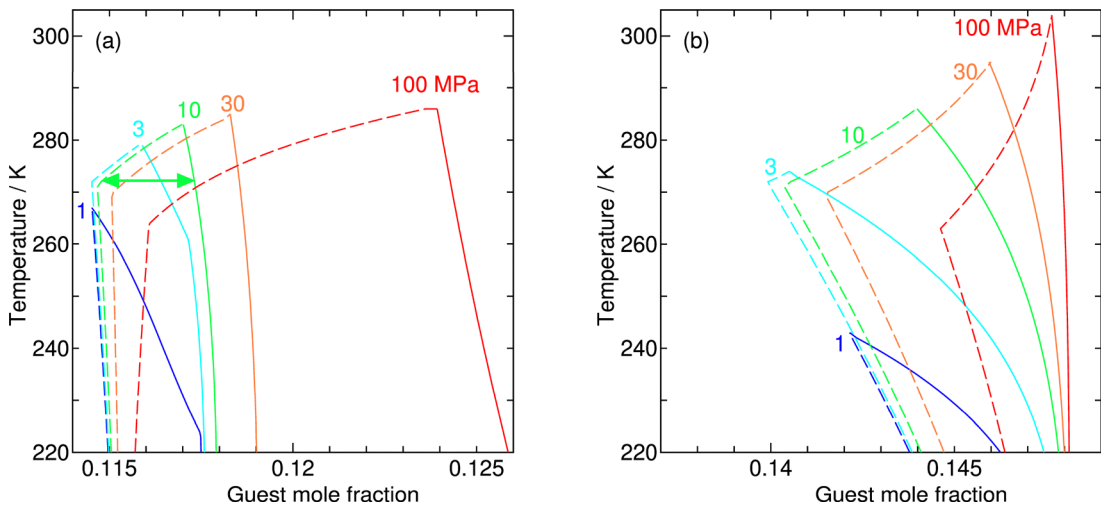

Fig. 6 Phase boundaries of (a) CO_2 and (b) CH_4 hydrates with the guest fluid (solid line) and water (dashed line) on the temperature–composition diagram at 1 (blue), 3 (cyan), 10 (green), 30 (orange) and 100 (red) MPa. The green bidirectional arrow denotes the composition range where the CO_2 hydrate alone is stable at 273 K and 10 MPa.

The phase diagram shown in Fig. 6a is helpful to explore the origin of the change in the solubility upon formation of CO_2 hydrate below the dissociation temperature, as represented in Fig. 3. The chemical potential of water decreases moving from the water/hydrate boundary to the hydrate/CO_2 boundary along the green arrow in Fig. 6, *i.e.*, $\Delta\mu_w^{(hy)} < 0$ in eqn (5). The chemical potential of CO_2 decreases ($\Delta\mu_c^{(hy)} < 0$ in eqn (7)) moving in the opposite direction. The magnitudes of the changes in the chemical potentials are constrained by the Gibbs–Duhem equation as

$$(1 - y_c)\frac{\partial\mu_w^{(hy)}}{\partial y_c} + y_c\frac{\partial\mu_c^{(hy)}}{\partial y_c} = 0, \quad (19)$$

which implies that $\left|\frac{\partial\mu_w^{(hy)}}{\partial y_c}\right|$ is smaller than $\left|\frac{\partial\mu_c^{(hy)}}{\partial y_c}\right|$ because y_c is smaller than 0.15 for CS-I hydrate, ruling out the multiple occupancy of cages. This relation, together with eqn (8), explains why the change in the solubility of water upon formation of hydrate is smaller than that of CO_2. In fact, the difference in the chemical potentials between the two boundaries for CO_2, $|\Delta\mu_c^{(hy)}|$, is several times larger than that for water, $|\Delta\mu_w^{(hy)}|$, as tabulated in Table 2. The chemical potential difference plays a decisive role in determining the magnitude of the effect of hydrate formation on the solubility.

The composition of a hydrate is associated with partial filling of each cage. The occupancies for the individual cage types are calculated according to eqn (11). The occupancy substantially depends on the cage types, guest species, and thermodynamic conditions, as depicted in Fig. 7. Compression and/or cooling enhance the occupancies. The occupancies at two pressures for the large cage in CO_2 hydrate nearly overlap each other. The large cages are more preferentially occupied in both CO_2 and CH_4 hydrates, although the magnitudes of the preference are different. While the large cages are almost fully occupied in CO_2 hydrate so as to lower the chemical potential of water according to eqn (10), the small cages are of little use to stabilise the hydrate. This is in sharp contrast to the stabilization mechanism of CH_4 hydrate, where both the large and small cages contribute to decrease the chemical potential of water in the hydrate.

Table 2 Chemical potential differences between the two boundaries for CO_2, $\Delta\mu_c^{(hy)}$, and for water, $\Delta\mu_w^{(hy)}$, at 10 MPa

T/K	$\Delta\mu_c^{(hy)}$/kJ mol^{-1}	$\Delta\mu_w^{(hy)}$/kJ mol^{-1}
273	−2.03	−0.32
277	−1.25	−0.22
281	−0.44	−0.11

The preferential occupation of the large cages by CO_2 molecules is substantiated by the orientationally averaged interaction energy of a guest with the surrounding water molecules, $\psi_j'(r)$, against the radial distance, r, from the cage center defined as

$$\psi_j'(r) = \frac{\int\int\psi_j(\mathbf{R},\mathbf{\Omega})\delta(|\mathbf{R}| - r)\mathrm{d}\mathbf{R}\mathrm{d}\mathbf{\Omega}}{\int\int\delta(|\mathbf{R}| - r)\mathrm{d}\mathbf{R}\mathrm{d}\mathbf{\Omega}}. \quad (20)$$

It is depicted in Fig. 8a, along with the resultant temperature dependences of the free energies of cage occupation in Fig. 8b. It is evident that a CO_2 molecule in the small cage has a higher interaction energy than that in the large cage due to its large molecular size. This leads to a much higher free energy of cage occupation, as shown in Fig. 8b. A CH_4 molecule in a small cage is stabilized by the surrounding water to a similar extent as that in large cage. Consequently, the difference in the free energy of occupation between them is small.

Precipitation of CO_2 hydrate under rapid cooling or decompression

Our main concern is the phase behaviour of liquid CO_2 with an impurity of water, which corresponds to the region near $z_c = 1$

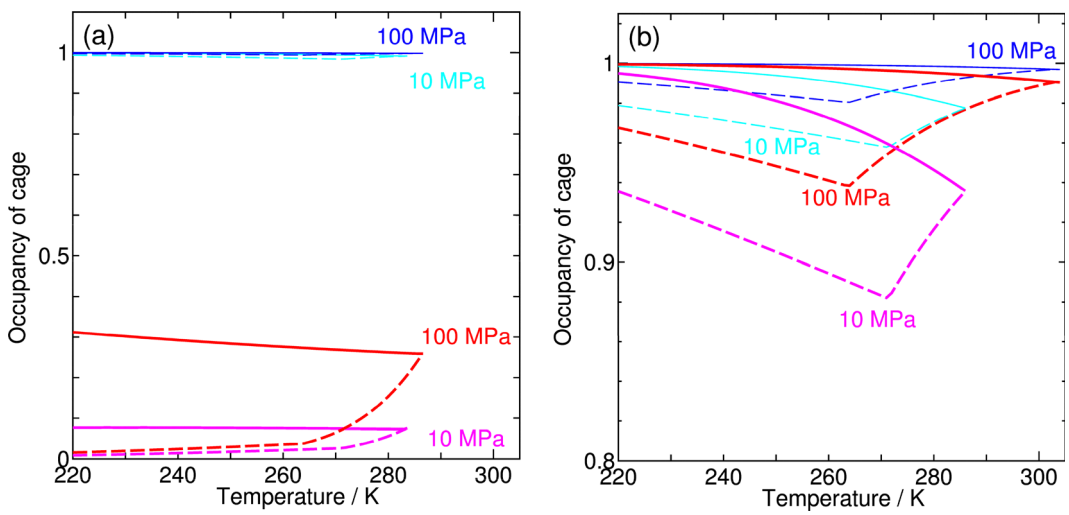

Fig. 7 Temperature dependence of cage occupancies for (a) CO_2 and (b) CH_4 hydrates at 10 (cyan: large, magenta: small) and 100 (blue: large, red: small) MPa. The solid and dashed lines represent the hydrate/guest and water/hydrate boundaries, respectively.

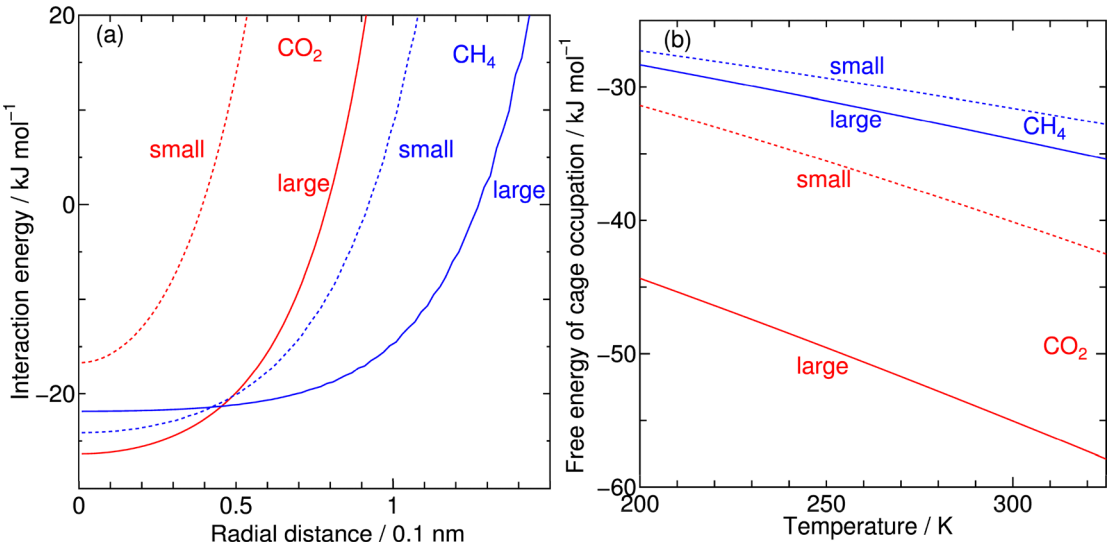

Fig. 8 (a) Orientationally averaged interaction energy of a guest with surrounding water molecules plotted against the radial distance from the cage center. (b) Free energies of cage occupation of (red) CO_2 and (blue) CH_4 for the (solid line) large and (dotted line) small cages.

in Fig. 2. The magnified temperature–composition diagram is depicted in Fig. 9. The diagram is divided into three regions, liquid (including gaseous) CO_2 with a small amount of dissolved water, liquid CO_2 coexisting with the hydrate (hydrate/CO_2), and liquid CO_2 coexisting with the aqueous solution (water/CO_2). The regions are separated by the dotted line corresponding to the dissociation temperature of the hydrate and by the solid line corresponding to the solubility of water. The phase diagram is also shown in Fig. S2 for each pressure.

The liquid CO_2 phase is in equilibrium with the aqueous solution at higher temperatures in the left region separated by the solubility curve in Fig. 9. The solubility of water in liquid CO_2, $z''_w = (1 - z''_c)$, decreases with decreasing temperature. Compression generally gives rise to a higher solubility of water. The curve at 10 MPa is nearly vertical around 310 K. This behaviour originates from the critical point of CO_2 (304.2 K and 7.38 MPa) around which the density changes strongly. At 5 MPa, CO_2 undergoes the phase transition from the liquid state to the gaseous one. This accompanies a sudden decline of the solubility, as illustrated in Fig. 9 where these two adjacent points are smoothly connected by the solid curve but the phase

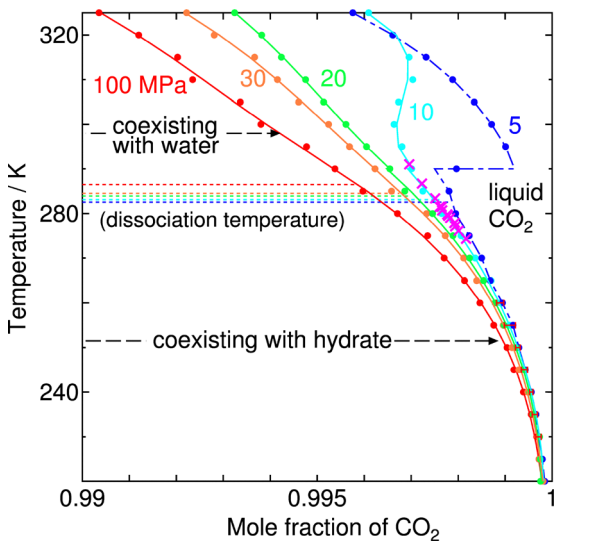

Fig. 9 Magnified phase diagram of the binary mixture of water and CO_2 for a region close to pure CO_2 at 5 (blue), 10 (cyan), 20 (green), 30 (orange), and 100 MPa (red). The stable region of fluid CO_2 is separated by the solid curve. Liquid CO_2 coexists with either the aqueous solution or CO_2 hydrate in the left region of each solid curve. Each dotted line indicates the dissociation temperature above which no hydrate is stable and the CO_2 fluid is in equilibrium with the aqueous solution. The blue dot-dash line depicts the interpolated solubility curve taking into account the breaks due to the vaporization of liquid CO_2 at 5 MPa. The magenta crosses denote the experimental solubilities at 10.1 MPa.[22]

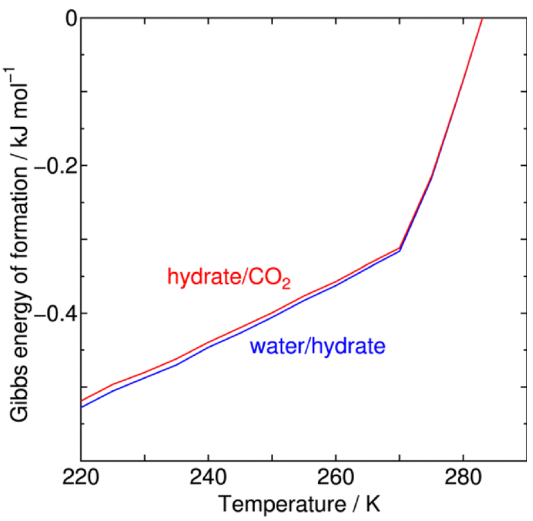

Fig. 10 Gibbs energy of formation of CO_2 hydrate *versus* temperature at a pressure of 10 MPa on the hydrate/CO_2 (red) and water/hydrate (blue) boundaries.

transition is represented by the dash-dot curve. The solubility of water in the gaseous CO_2 phase is the vapor pressure of pure liquid water to a good approximation and therefore is expected to decrease with compression, according to the present definition of the solubility given by eqn (3), through an increase in $\rho^{(k)}$.

The Gibbs energy difference between the reactants (water and CO_2) and the product (hydrate) plays an essential role in determining the rate of hydrate formation. It is also known as the thermodynamic driving force for the formation of hydrate and has been calculated with available thermodynamic properties from MD simulations.[37,38] We have shown that it can also be calculated in a relatively simple way from the chemical potentials, which are available from the method we developed.[16] The Gibbs energy of formation in our definition is measured on a per water molecule (mole) basis, reflecting the non-stoichiometric nature of hydrate. As stated above, we make a slightly rough approximation for the chemical potentials of water and CO_2 such that water in hydrate on the water/hydrate boundary has the same chemical potential of pure water, although it contains a certain amount of CO_2, and the guest species in the hydrate on the hydrate/CO_2 boundary has the same chemical potential of pure CO_2. The Gibbs energy of formation at a composition of y_c is given as

$$\Delta G_f = \mu_w^{(hy)}(T,p,y_c) - \mu_w^0(T,p) + \frac{y_c}{1-y_c}\left[\mu_c^{(hy)}(T,p,y_c) - \mu_c^0(T,p)\right]. \quad (21)$$

This quantity converges to zero on approaching the three-phase equilibrium. There are two extreme cases for the composition of the product hydrate, y_c. In the first one, we consider formation of the hydrate under a water-rich condition, *i.e.*, on the water/hydrate boundary where the composition of the guest in the hydrate is y_c'. The Gibbs energy of formation is given by

$$\Delta G_f = \frac{y_c'}{1-y_c'}\left[\mu_c^{(hy)}(T,p,y_c') - \mu_c^0(T,p)\right]. \quad (22)$$

This is plotted against temperature in Fig. 10. In the second, the hydrate is assumed to be formed under a guest-rich condition on the hydrate/guest boundary at a composition of y_c''. The Gibbs energy of formation is given by

$$\Delta G_f = \mu_w^{(hy)}(T,p,y_c'') - \mu_w^0(T,p). \quad (23)$$

This is also shown in Fig. 10. It differs only slightly from that found according to eqn (22).

Thus far, the initial state was chosen to be pure water and CO_2 at a given temperature and pressure. We can consider a different formation process in which the initial state is liquid CO_2 supersaturated with water prepared by a temperature drop. This process is schematically drawn in Fig. 11. The temperature is dropped vertically from a certain point on the phase boundary to a point below the dissociation temperature of CO_2

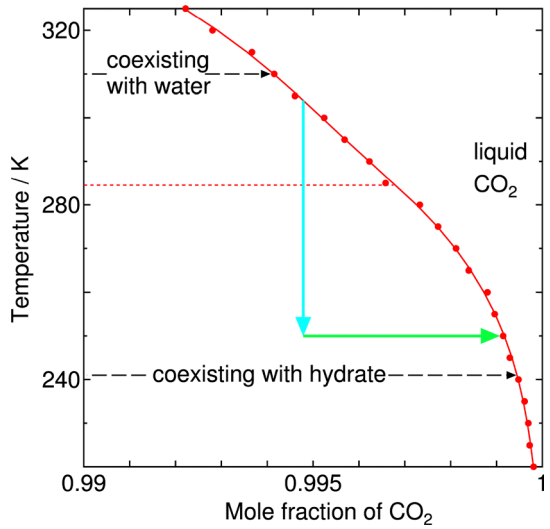

Fig. 11 Isobaric cooling in the temperature–composition diagram. The red solid and dotted lines indicate the phase boundary of liquid CO_2 and the dissociation temperatures of CO_2 hydrate. The temperature is dropped along the vertical line from a point on the red solid curve to an arbitrary temperature, T in eqn (24).

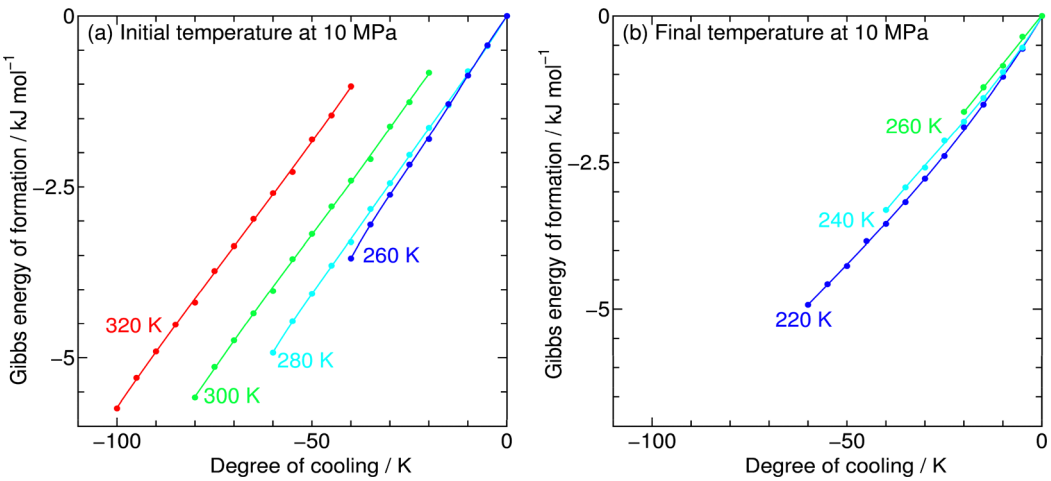

Fig. 12 Gibbs energy of formation of CO_2 hydrate plotted against the degree of cooling at 10 MPa for (a) four initial temperatures and (b) three final temperatures.

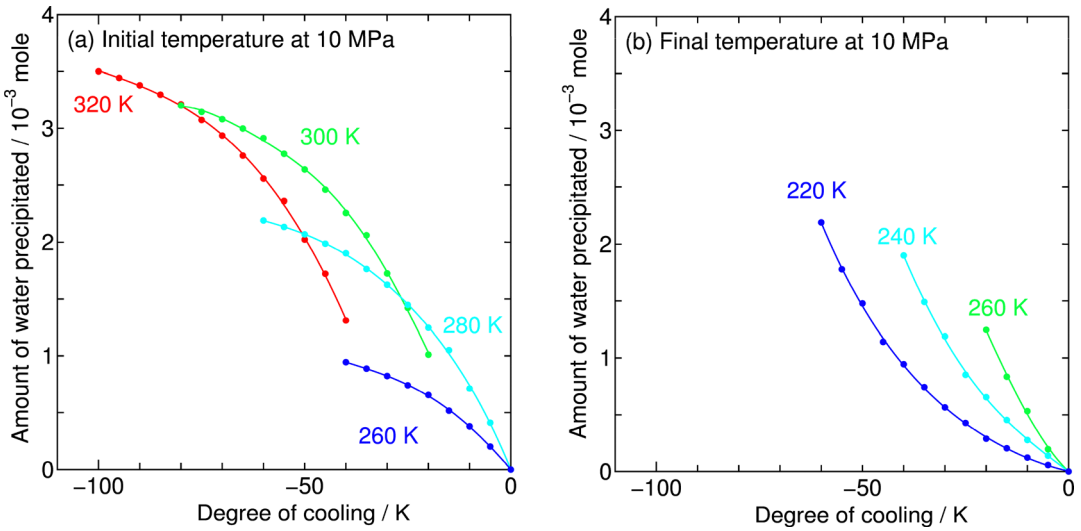

Fig. 13 Amount of wate precipitated as hydrate from one mole of liquid CO_2 at 10 MPa, plotted against the degree of cooling for (a) four initial temperatures and (b) three final temperatures.

hydrate. Consequently, an excessive amount of water precipitates as CO_2 hydrate.

The liquid CO_2 at the initial state contains a certain amount of saturated water whose density is ρ_w or an equivalent composition of the corresponding solubility, z_c. Since $\mu_w^0(T,p)$ in eqn (23) should be replaced with $\mu_w^{(lq)}(T,p,z_c)$ in this process, the Gibbs energy of formation is calculated from $\mu_w^{(hy)}(T,p,y_c'') = \mu_w^{(lq)}(T,p,z_c'')$ as

$$\Delta G_f = \mu_w^{(hy)}(T,p,y_c'') - \mu_w^{(lq)}(T,p,z_c) = \mu_w^{(lq)}(T,p,z_c'') - \mu_w^{(lq)}(T,p,z_c) = k_B T \ln\left(\frac{\rho_w''}{\rho_w}\right), \quad (24)$$

where ρ_w'' is the equilibrium density of water in liquid CO_2 coexisting with CO_2 hydrate at T and p.

This Gibbs energy of formation, the sign of which is limited to negative, is depicted as a function of the degree of cooling in Fig. 12 for (a) the initial temperature from which liquid CO_2 undergoes rapid cooling and (b) the final one to which it will be settled. It decreases as the degree of cooling or equivalently the supersaturation is intensified. In other words, supersaturation significantly induces formation of CO_2 hydrate to achieve equilibrium between hydrate and liquid CO_2 at the final temperature. The Gibbs energy change is almost linear in both panels. A higher initial temperature requires a deeper cooling to have the same energy value as is seen in panel (a). CO_2 hydrate does not appear at 300 or 320 K at a pressure of 10 MPa, and therefore the corresponding curves shift to the left side. The Gibbs energies for the various final temperatures seem to be laid on a common straight line passing through the origin in panel (b) under the fixed final temperature condition.

Another intriguing quantity from an industrial viewpoint is the amount of hydrate precipitated from liquid CO_2 supersaturated with water. The formation of hydrate incurs the blockage of pipelines in liquid CO_2 transportation. The amount of hydrate from one mole of liquid CO_2 is plotted in Fig. 13 as a function of temperature drop. Again, we examine it for either (a) the initial temperature from which liquid CO_2 is cooled down or (b) the final one to which it will be settled. As plotted in Fig. 13a, the amount of water increases simply with the extent of cooling, but the relation between the amount and the initial temperature at a given degree of cooling is complicated. However, the amount simply decreases with decreasing final temperature at a given degree of cooling, as seen in Fig. 13b.

Next, we consider a pressure drop of liquid CO_2. This may also happen in a pipeline going downstream. Here, we assume the pressure drop takes place isothermally, as drawn in Fig. 14. We calculate the amount of hydrate precipitated in this process

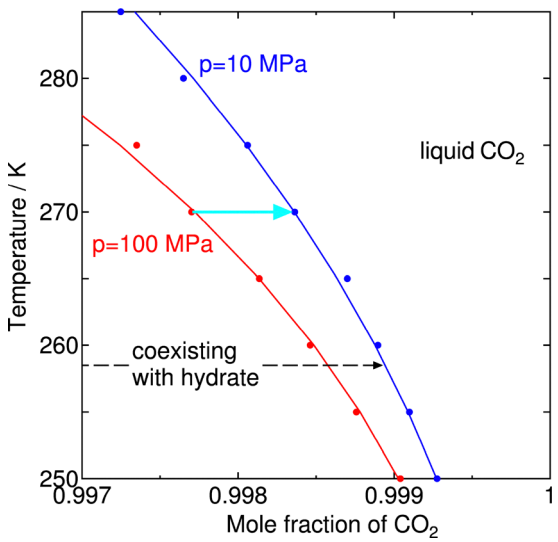

Fig. 14 Isothermal decompression in the temperature–composition diagram. The red and blue solid lines indicate the phase boundaries of liquid CO_2. The pressure drops along the horizontal line from an initial point on the red curve to the final point on the blue curve.

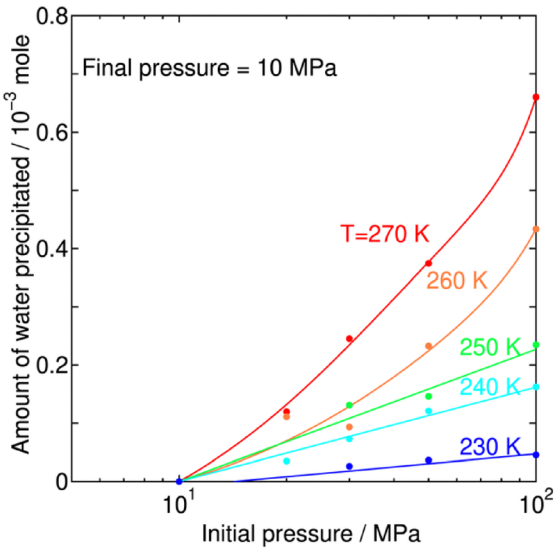

Fig. 15 Amount of water precipitated as hydrate from one mole of liquid CO_2 by rapid decompression to a final pressure of 10 MPa, plotted against the initial pressure at 230 (blue), 240 (cyan), 250 (green), 260 (orange), and 270 K (red).

in the same way as in the case of the temperature drop. The amount of precipitation due to decompression is shown in Fig. 15. The amount is small compared with that of the cooling process even when the initial pressure is an order magnitude larger than the final pressure. As is expected from Fig. 9, the precipitation amount becomes larger with increasing temperature.

Conclusions

The solubility of water in liquid CO_2 is calculated using atomistic intermolecular potential models. Liquid CO_2 coexists with liquid water and CO_2 hydrate above and below the dissociation temperature of the hydrate, respectively. The solubility of water in liquid CO_2 increases with increasing temperature, and compression enhances the solubility regardless of the presence or absence of hydrate.

Several properties of CO_2 hydrate are examined, focusing on the water/hydrate and hydrate/CO_2 two-phase coexistences. Whereas CH_4 hydrate is stabilised by moderate occupancy of large cages and the same degree of occupancy of small cages, the stability of CO_2 hydrate is mostly due to the preferential occupation of large cages.

CO_2 hydrate forms not only by a temperature drop but also by a pressure drop of liquid CO_2 containing water as an impurity. The amount is seemingly small but can pose the risk of pipeline blockage. Another important factor for flow assurance is the nucleation kinetics of CO_2 hydrate, but that is out of the scope of the present study.

The temperature and pressure ranges differ for each operational condition. The solubility of water and the amount of precipitated hydrate are heavily dependent on temperature and pressure. Hence, the allowable content of water in liquid CO_2 may be set flexibly, avoiding overly conservative constraints. The Gibbs energy of formation and the associated properties in the present study are expected to provide a valuable insight into the conditions for safe CO_2 transportation without hydrate formation.

Author contributions

Hideki Tanaka: conceptualization, methodology, investigation, interpretation, and writing – original draft. Masakazu Matsumoto: methodology, constructive discussions, writing – review and editing, and funding acquisition. Takuma Yagasaki: methodology, interpretation, constructive discussions, and writing – review and editing. Munetaka Takeuchi: constructive discussions, interpretation, and writing – review and editing. Yoshihito Mori: constructive discussions, interpretation, and writing – review and editing. Takumi Kono: constructive discussions, project administration, and funding acquisition.

Conflicts of interest

The authors have no conflicts to disclose.

Data availability

The data that support the findings of this study are available from the corresponding author upon reasonable request. All relevant figures are included in the supplementary information (SI). Supplementary information is available. See DOI: https://doi.org/10.1039/d6cp01072e.

Acknowledgements

The present work is supported by JSPS KAKENHI (Grant Number: 23K20830) and the Research Center for Computational Science for providing computational resources (Project: 23-IMS-C028).

References

1 G. Brunner, *Gas Extraction*, Springer, New York, 1991.
2 S. Angus, B. Armstrong and K. M. de Reuck, *International Thermodynamic Tables of the Fluid State – Carbon Dioxide*, 1976.
3 Thermophysical properties of fluid systems, NIST Chemistry Webbook (National Institute of Standards and Technology), 2025, https://webbook.nist.gov/chemistry/, (accessed March 16, 2026).
4 N. MacDowell, N. Florin, A. Buchard, J. Hallett, A. Galindo, G. Jackson, C. S. Adjiman, C. K. Williams, N. Shah and P. Fennell, *Energy Environ. Sci.*, 2010, **3**, 1645–1669.
5 T. Kuznetsova, B. Jensen, B. Kvamme and S. Sjøblom, *Phys. Chem. Chem. Phys.*, 2015, **17**, 12683–12697.
6 T. Yagasaki, M. Matsumoto and H. Tanaka, *J. Am. Chem. Soc.*, 2015, **137**, 12079–12085.
7 M. A. Kelland, *Energy Fuels*, 2018, **32**, 12001–12012.

8 M. Aminnaji, M.-F. Qureshi, H. Dashti, A. Hase, A. Mosalanejad, A. Jahanbakhsh, M. Babaei, A. Amiri and M. Maroto-Valer, *Energy*, 2024, **300**, 131579.
9 M. Aminnaji, M.-F. Qureshi, H. Dashti, A. Hase, A. Mosalanejad, A. Jahanbakhsh, M. Babaei, A. Amiri and M. Maroto-Valer, *Energy*, 2024, **300**, 131580.
10 M. A. Kelland and J. Pomicpic, *Energy Fuels*, 2025, **39**, 9802–9817.
11 E. D. Sloan and C. A. Koh, *Clathrate Hydrates of Natural Gases*, CPC Press, Boca Raton, 2008.
12 H. Tanaka, T. Yagasaki and M. Matsumoto, *J. Phys. Chem. B*, 2018, **122**, 297–305.
13 H. Tanaka, T. Yagasaki and M. Matsumoto, *J. Chem. Phys.*, 2018, **149**, 074502.
14 H. Tanaka, M. Matsumoto and T. Yagasaki, *J. Chem. Phys.*, 2023, **158**, 224502.
15 H. Tanaka, M. Matsumoto and T. Yagasaki, *J. Chem. Phys.*, 2023, **159**, 194504.
16 H. Tanaka, M. Matsumoto and T. Yagasaki, *J. Chem. Phys.*, 2024, **161**, 214503.
17 H. Tanaka, M. Matsumoto, T. Yagasaki, M. Takeuchi, Y. Mori and T. Kono, *J. Chem. Phys.*, 2025, **163**, 124504.
18 T. Yagasaki, M. Matsumoto and H. Tanaka, *J. Chem. Phys.*, 2026, **164**, 020901.
19 J. H. van der Waals and J. C. Platteeuw, *Adv. Chem. Phys.*, 1959, **2**, 1–57.
20 J. I. Lunine and D. J. Stevenson, *Astrophys. J., Suppl. Ser.*, 1985, **58**, 493–531.
21 H. Tanaka and M. Matsumoto, *Adv. Chem. Phys.*, 2013, **152**, 421–462.
22 M. D. Seo, J. W. Kang and C. S. Lee, *J. Chem. Eng. Data*, 2011, **56**, 2626–2629.
23 I. Aavatsmark and R. Kaufmann, *Int. J. Greenhouse Gas Control*, 2015, **32**, 47–55.
24 E. Wilhelm, R. Battino and R. Wilcock, *Chem. Rev.*, 1977, **77**, 219–262.
25 R. Crovetto, *J. Phys. Chem. Ref. Data*, 1991, **20**, 575–589.
26 C. H. Unruh and D. L. Katz, *Trans. AIME*, 1949, **186**, 83–86.
27 S. Takenouchi and G. C. Kennedy, *J. Geol.*, 1965, **73**, 383–390.
28 S. Nakano, M. Moritoki and K. Ohgaki, *J. Chem. Eng. Data*, 1998, **43**, 807–810.
29 J. L. F. Abascal, E. Sanz, R. García Fernández and C. Vega, *J. Chem. Phys.*, 2005, **122**, 234511.
30 J. J. Potoff and J. I. Siepmann, *AIChE J.*, 2001, **47**, 1676–1682.
31 B. Widom, *J. Chem. Phys.*, 1963, **39**, 2808.
32 S. Nosé, *Mol. Phys.*, 1984, **52**, 255–268.
33 W. G. Hoover, *Phys. Rev. A:At., Mol., Opt. Phys.*, 1985, **31**, 1695–1697.
34 H. C. Andersen, *J. Chem. Phys.*, 1980, **72**, 2384–2393.
35 I. Ohmine, H. Tanaka and P. G. Wolynes, *J. Chem. Phys.*, 1988, **89**, 5852–5860.
36 A. Pohorille, L. R. Pratt, R. A. LaViolette, M. A. Wilson and R. D. MacElroy, *J. Chem. Phys.*, 1987, **87**, 6070–6077.
37 J. Grabowska, S. Blazquez, E. Sanz, I. M. Zerón, J. Algaba, J. M. Míguez, F. J. Blas and C. Vega, *J. Phys. Chem. B*, 2022, **126**, 8553–8570.
38 J. Algaba, I. M. Zerón, J. M. Míguez, J. Grabowska, S. Blazquez, E. Sanz, C. Vega and F. J. Blas, *J. Chem. Phys.*, 2023, **158**, 184703.
39 W. L. Jorgensen, J. D. Madura and C. J. Swenson, *J. Am. Chem. Soc.*, 1984, **106**, 6638–6646.
40 G. Pérez-Sánchez, D. González-Salgado, M. M. Piñeiro and C. Vega, *J. Chem. Phys.*, 2013, **138**, 084506.
41 H. Tanaka, M. Matsumoto, T. Yagasaki, M. Takeuchi, Y. Mori and T. Kono, *J. Chem. Phys.*, 2024, **158**, 224502.
42 M. M. Conde and C. Vega, *J. Chem. Phys.*, 2010, **133**, 064507.
43 J. M. Míguez, M. M. Conde, J.-P. Torré, F. J. Blas, M. M. Piñeiro and C. Vega, *J. Chem. Phys.*, 2015, **142**, 124505.
44 J. Grabowska, S. Blazquez, E. Sanz, I. M. Zerón, J. Algaba, J. M. Míguez, F. J. Blas and C. Vega, *J. Phys. Chem. B*, 2022, **126**, 8553–8564.
45 M. Matsumoto, T. Yagasaki and H. Tanaka, *J. Comput. Chem.*, 2018, **39**, 61–64.
46 M. Matsumoto, T. Yagasaki and H. Tanaka, *J. Chem. Inf. Model.*, 2021, **61**, 2542–2546.
47 J. D. Bernal and R. H. Fowler, *J. Chem. Phys.*, 1933, **1**, 515–548.
48 L. Pauling, *J. Am. Chem. Soc.*, 1935, **57**, 2680–2684.
49 I. Aya, K. Yamane and H. Nariai, *Energy*, 1997, **22**, 263–271.
50 P. Servio and P. Englezos, *Fluid Phase Equilib.*, 2001, **90**, 127–134.
51 A. Chapoy, R. Burgass, B. Tohidi, J. M. Austell and C. Eickhoff, *SPE J.*, 2011, **16**, 921–930.
52 J. Gernert and R. Span, *J. Chem. Thermodyn.*, 2016, **93**, 274–293.
53 T. Uchida, *Waste Manage.*, 1997, **17**, 343–352.
54 A. Hachikubo, M. Kida, D. Yahagi and S. Takeya, *Energy Fuels*, 2024, **38**, 9676–9682.
55 S. C. Velaga and B. J. Anderson, *J. Phys. Chem. B*, 2014, **118**, 577–589.